# Distributed Acoustic Sensing Recordings of Cryoseismicity Enable Seismic Imaging of Permafrost in Remote Arctic Regions

Ahmad Tourei[1,2*], Eileen R. Martin[1,2], Gabriel Rocha dos Santos[3], Tieyuan Zhu[3], Nikhil Punithan[2], Ming Xiao[4]

[1]Hydrologic Science and Engineering Program, Colorado School of Mines, Golden, CO, USA
[2]Department of Geophysics, Colorado School of Mines, Golden, CO, USA
[3]Department of Geosciences, Pennsylvania State University, University Park, PA, USA
[4]Department of Civil and Environmental Engineering, Pennsylvania State University, University

* Corresponding author contact: tourei@mines.edu

This Express Letter is submitted to *Geophysical Journal International* for peer review and potential publication.

submitted to *Geophys. J. Int.*

# Distributed Acoustic Sensing Recordings of Cryoseismicity Enable Seismic Imaging of Permafrost in Remote Arctic Regions

Ahmad Tourei[1,2⋆], Eileen R. Martin[1,2], Gabriel Rocha dos Santos[3], Tieyuan Zhu[3], Nikhil Punithan[2], Ming Xiao[4]

[1]*Hydrologic Science and Engineering Program, Colorado School of Mines, Golden, CO, USA*

[2]*Department of Geophysics, Colorado School of Mines, Golden, CO, USA*

[3]*Department of Geosciences, Pennsylvania State University, University Park, PA, USA*

[4]*Department of Civil and Environmental Engineering, Pennsylvania State University, University Park, PA, USA*

Received 2026 July XX; in original form 2026 July XX

**SUMMARY**

Permafrost can be highly heterogeneous, and variability in its subsurface structure under climate warming remains poorly understood despite the critical role of permafrost in Arctic hydrology, ecosystems, and infrastructure stability. Distributed acoustic sensing (DAS) provides a long-term method for dense seismic array monitoring in remote regions with passively recorded seismic activities.We deployed a 2 km fiber-optic DAS array across disturbed and undisturbed tundra near Utqiagvik, Alaska. It recorded naturally occurring cryoseismic events generated by shallow thermal contraction cracking. These events fill data gaps and provide seismic energy for imaging subsurface permafrost structure. We assessed the effects of gauge length and wave-propagation direction on the extracted dispersion characteristics and evaluated the stability and uncertainty of the resulting shear-wave velocity (Vs) inversions. The resulting Vs models reveal deep ice-rich layers interpreted as massive ground ice. This demonstrates a new, scalable technique for permafrost characterization using cryoseismic energy, which may have potential for time-lapse monitoring of permafrost dynamics and supporting infrastructure resilience in remote regions.

**Key words:** Arctic Region – Cryoseismology – Distributed Acoustic Sensing

## 1 INTRODUCTION

Permafrost is a key component of the cryosphere and plays a crucial role in maintaining the stability of Arctic ecosystems and ensuring the integrity of infrastructure (Hjort et al., 2022). Permafrost is often highly heterogeneous due to variations in ice content, grain size, salinity, and moisture distribution, all of which influence its thermal and mechanical behaviors (Tourei et al., 2024a; Wu et al., 2017). With accelerating climate warming, thawing permafrost leads to rapid changes in subsurface structure, including ice thaw, pore pressure buildup, and subsidence. Near-surface shear-wave velocity (Vs) profiling provides key insights into subsurface mechanical properties (Babaee et al., 2025; Socco & Strobbia, 2004). High-resolution imaging is crucial to capture subsurface changes, quantify degradation rates, and improve permafrost stability predictions, as many permafrost processes occur on the meter to tens-of-meter scales. However, repeated active-source surveys in remote Arctic regions are logistically challenging, costly, and can disturb sensitive tundra conditions, so we are motivated to monitor subsurface structures through passively recorded energy. Further, geophone and nodal arrays require logistics and support costs that are infeasible for multi-year or multi-decadal monitoring needs. From both the source and sensor perspective, permafrost characterization suffers from a major data gap.

Distributed acoustic sensing (DAS) enables continuous permafrost monitoring with dense spatial coverage over kilometer-scale fiber-optic cables (Cheng et al., 2022; Wagner et al., 2018). Where seismic noise distributions are appropriate, it can be integrated with ambient noise interferometry to image subsurface structure and evolution (Dou et al., 2017; Rodríguez Tribaldos & Ajo-Franklin, 2021; Wapenaar et al., 2010). However, passive seismic monitoring often lacks sufficient high-frequency energy to resolve shallow layers (Dangwal et al., 2023). Particularly, low

⋆ Corresponding author. E-mail: ahmadtourei@gmail.com

ambient noise levels in winter in remote regions can limit stability of Green's functions, inhibiting time-lapse monitoring. Passive DAS monitoring in Arctic environments is challenged by weak seismic energy, anisotropic noise fields, fiber installation challenges, and signal attenuation in heterogeneous ground, which reduces waveform coherence and amplitude interpretation (Castongia et al., 2017; Harmon et al., 2022; Sun et al., 2025). Turning from ambient noise, the other alternative for passive monitoring with DAS is to use a selection of naturally occurring seismic events. Because DAS can cover a large region with high resolution, many signals can be recorded as potential energy sources for imaging. However, fiber orientation and wave propagation characteristics are crucial to accurately using and interpreting any DAS-based passive event recordings. In surface wave recordings, DAS is particularly responsive to Rayleigh waves propagating along the cable, but can also introduce mode-dependent biases when compared to traditional vertical-component geophones (Martin, 2021; Luo et al., 2021; Yuan & Martin, 2025; Gribler et al., 2016; Shapiro et al., 2001; Viens et al., 2022).

Cryoseisms, or frost quakes, are seismic events that occur when rapid surface cooling causes frozen, water-saturated ground to contract and crack, releasing accumulated stress explosively (Barosh, 2000). These shallow events generate strong surface waves and may be accompanied by audible cracking or booming sounds, but their seismic energy decays quickly with distance (Leung et al., 2017; Nikonov, 2010). A recent study in Adventdalen, Svalbard by Romeyn et al. (2021) has demonstrated the potential of cryoseismic and surface-wave analyses to characterize near-surface permafrost structure and dynamics. Passive seismic recordings of cryoseisms in Adventdalen revealed that frost-quake events generate strong surface-wave energy, enabling multichannel analysis of surface waves (MASW), a non-invasive monitoring technique, to delineate ice-rich layers within the active layer and upper permafrost (Romeyn et al., 2021). Similarly, long-term cryoseismic catalogs derived from the smaller-aperture Spitsbergen seismic array highlight the sensitivity of ground thermal stress and frost cracking to environmental forcing (Romeyn et al., 2022).

Ice content strongly controls permafrost strength, making seismic velocity a sensitive tool for mapping ground ice distribution (Akhtarshenas et al., 2024; Wu et al., 2017; Ji et al., 2024). However, inverting surface-wave dispersion in permafrost is challenging due to strong velocity contrasts and lateral heterogeneity, which can lead to non-unique or unstable solutions. Linearized inversion methods are computationally efficient but sensitive to the initial model (Wang et al., 2022). Nonlinear approaches better capture complex velocity structures and parameter trade-offs but may converge to local minima and provide limited uncertainty estimates (Xia et al., 1999). To overcome these limitations, stochastic global search methods such as grid search, Monte Carlo, genetic algorithms, and neighborhood algorithms are used to explore broader model spaces and quantify uncertainty (Lehujeur et al., 2021; Lomax & Snieder, 1994; Macquet et al., 2014; Maraschini & Foti, 2010; Mordret et al., 2014).

In this study, we use cryoseismic events recorded by DAS to image permafrost. We extract surface-wave dispersion curves from these passive events and apply a suite of MASW techniques with two inversion strategies to build Vs profiles. Furthermore, we analyze the effects of gauge length and wave propagation directionality on the resulting dispersion characteristics. By integrating DAS cryoseismic observations, inversion analyses, and insights from elastic wavefield modeling, we evaluate the feasibility, sensitivity, and limitations of this approach for permafrost characterization. We propose recommendations for optimal data acquisition and processing strategies to open up new opportunities that have the potential to greatly reduce the logistics and cost required for future permafrost monitoring campaigns.

## 2 STUDY SITE AND DATA ACQUISITION

The DAS dataset was collected from a continuous passive field experiment conducted near Utqiaġvik, Alaska on the Arctic Coastal Plain, approximately 2 km inland from the coastline (Fig. 1). The region is underlain by continuous permafrost extending 200–400 m deep (Jorgenson et al., 2008), with an active layer ranging from 0.2 m to 0.3 m (Tourei et al., 2024a). A 2 km-long DAS array was installed in August 2021, originating at the Department of Energy (DOE) Atmospheric Radiation Measurement (ARM) facility, running alongside a road near a National Oceanic and Atmospheric Administration (NOAA) building, and extending northeast toward Elson Lagoon. The route crossed undisturbed tundra and disturbed permafrost zones associated with infrastructure. The fiber-optic cable was manually installed by inserting a shovel to create a shallow opening

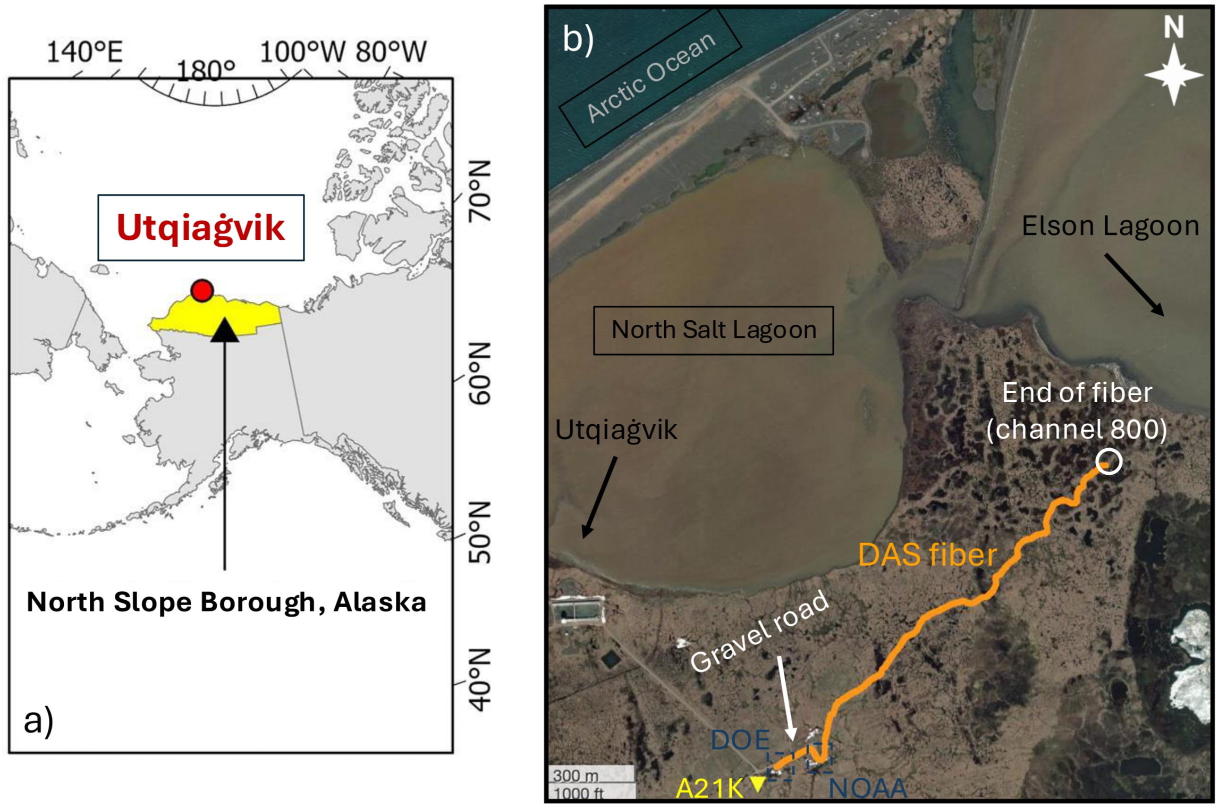


**Figure 1.** Map of the North Slope Borough, Alaska (a) and the study site northeast of Utqiaġvik (b), showing fiber-optic cable route (in orange) and the A21K seismometer (yellow triangle).

(about 30 centimeters) at the top of the permafrost table and placing the cable within it. The shovel was then removed, allowing the opening to close, and the soil was gently compacted to secure the cable and minimize surface disturbance. DAS data were collocated with borehole core samples, temperature boreholes, an electrical resistivity tomography survey, and five active-source geophone MASW surveys in August 2022 (Tourei et al., 2024a). We used a Treble Terra15 interrogator with a 500 Hz sampling rate and 2.45 m channel spacing. The fiber-optic cable recorded axial strain rate from ambient wavefields, including traffic (mainly from the road), earthquakes, seismic tremors from sea ice (Rocha dos Santos & Zhu, 2025b), and cryoseismic events potentially due to ice-wedge cracking (Rocha dos Santos & Zhu, 2025a).

## 3 DATA PROCESSING SCHEME

The penetration depth of surface waves is frequency-dependent; longer wavelengths (lower frequencies) sample deeper layers and shorter wavelengths (higher frequencies) are sensitive to near-surface layers, (Park et al., 1998). By analyzing the frequency and phase velocity relationship, the MASW method estimates the Vs structure of the subsurface. We initially applied seismic ambient noise interferometry to generate virtual shot gathers for dispersion analysis. However, the tundra near Utqiaġvik lacked sufficient continuous noise for stable noise correlation functions, and even three weeks of stacked data showed no coherent surface-wave arrivals. This limitation motivated the use of alternative energy sources for imaging. To discover new sources, we employed an autoencoder-based anomaly detection model (Tourei et al., 2024b) to identify anomalies, which were then investigated to find impulsive cryoseismic events that exhibit strong surface-wave energy. To extract dispersion curves, we applied the phase-shift method (Park et al., 1998).

Increasing the gauge length improves the signal-to-noise ratio (SNR) of DAS measurements but reduces spatial resolution. While applying a longer gauge length enhances the detectability of cryoseismic events by increasing the SNR, it limits the shortest measurable wavelength for a given wave speed (Vantassel et al., 2022). Fig. 2 illustrates the effect of gauge length selection on surface-wave characterization, showing that increasing the gauge length increases the strength of weak signals, but also reduces the fidelity of dispersion images at higher frequencies, thus increasing phase velocity uncertainty. This occurs because a longer gauge length averages strain rate over a greater fiber distance, effectively smoothing out high-frequency signals. The dashed lines on the dispersion images indicate the minimum and maximum wavelengths that can be reliably sampled based on the gauge length and total array aperture.

Prior to inversion analysis, we examined the recorded wavefield to determine the dominant surface-wave mode. Cryoseismic events are primarily tensile cracking phenomena, involving volumetric expansion and opening of frozen ground rather than shear displacement, which generates strong P- and SV-wave energy but minimal SH-wave energy (Afonin et al., 2024; Okkonen et al., 2020). Consequently, Love waves' transverse motion is expected to be weak or absent. Similar SV-wave polarization has been reported by frost-quake studies in Finland (Afonin et al., 2024). To confirm the dominant surface wavefield in our dataset, we analyzed waveforms from the nearby three-component AK-A21K broadband station (Fig. 1). We investigated two cryoseismic events in detail, which we refer to as Events 1 and 2. In Event 1 (Fig. 2a), the root-mean-square (RMS)

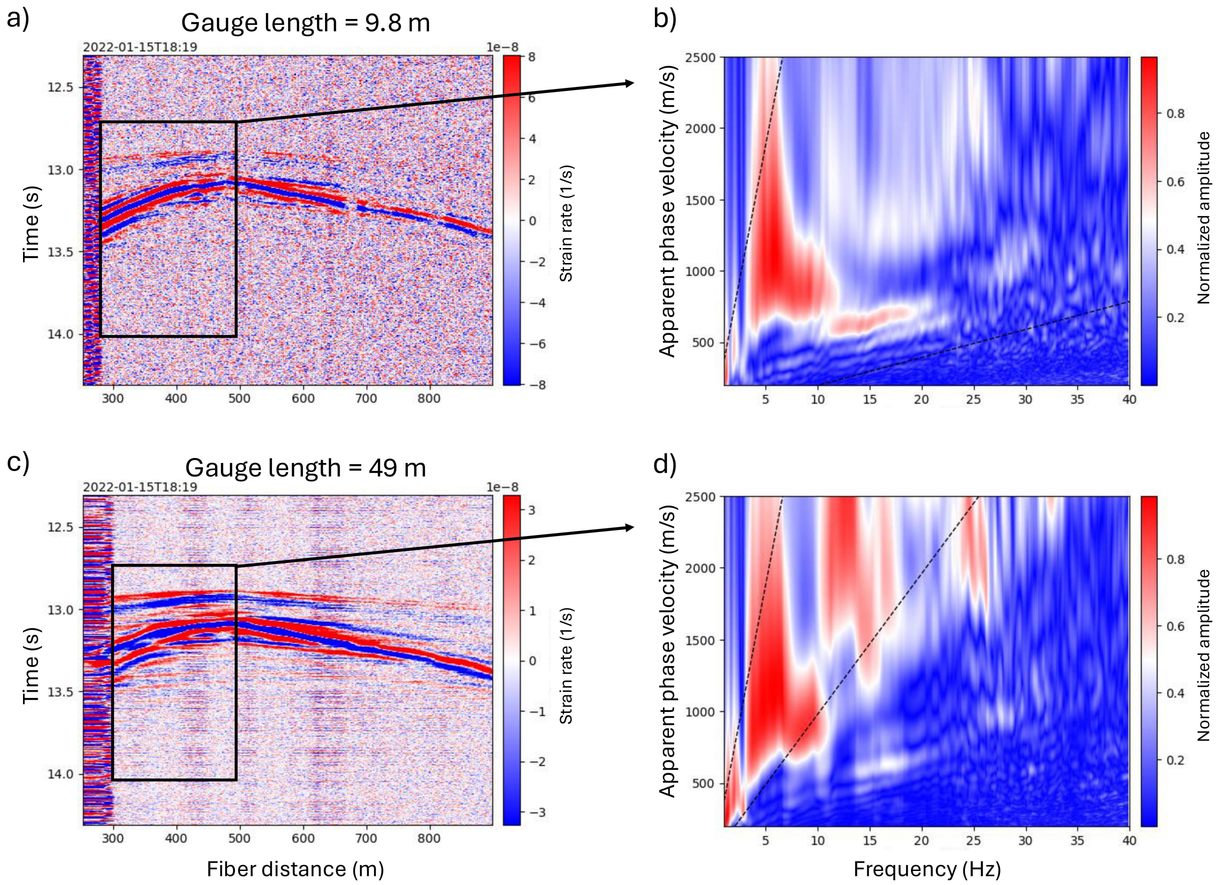


**Figure 2.** The time-domain raster plots (a and c) and the gauge length's effect on the dispersion results (b and d) for cryoseismic Event 1.

ratios between the horizontal and vertical components of surface-wave arrivals were 0.32 for N/Z and 0.27 for E/Z components, respectively. These low horizontal-to-vertical amplitude ratios indicate that the recorded energy is primarily associated with Rayleigh-type motion, consistent with the SV-polarized wavefields generated by tensile cracking sources. Thus, our subsequent dispersion analysis and inversion were performed under the assumption of Rayleigh-wave–dominated energy. Three-component data from station A21K were unavailable for Event 2.

Horizontal DAS arrays are inherently more sensitive to Rayleigh wave components with strong horizontal motion (i.e., large ellipticity), which can enhance the detection of higher-order modes that exhibit greater ellipticity than the fundamental mode (Fang et al., 2023; Shapiro et al., 2001; Viens et al., 2022). Figure S1 in the online supplementary material presents an additional cryoseismic event in which the fundamental and first higher-order modes are clearly identified. As a complementary assessment of Rayleigh-wave dominance, we applied a statistical version of horizontal-to-vertical spectral ratio (HVSR) analysis to AK-A21K data, which accounts for azimuthal variability (Cheng et al., 2020; Vantassel, 2025). In Event 1, HVSR values exceeding unity above 11 Hz are consistent with the separate moveout observed (Fig. 2b) and indicate increased ellipticity at higher frequencies. Additional details on the HVSR analysis are provided in the supplementary material, Figure and Text S2.

Inversion of Rayleigh-wave dispersion curves to estimate Vs profiles is inherently non-unique, as several subsurface models can reproduce the same dispersion curve within the data uncertainty. To understand the reliability of Vs profiles, we applied two inversion approaches: a deterministic non-linear least-squares (NLLS) method and a stochastic Monte Carlo (MC) global search. The NLLS inversion iteratively adjusts model parameters to minimize the difference between measured and calculated dispersion curves using the Levenberg–Marquardt algorithm (Xia et al., 1999). The forward dispersion modeling for NLLS was implemented using a global stiffness matrix formulation for layered elastic media following Kausel & Roësset (1981). In contrast, the MC inversion randomly samples combinations of layer thicknesses and velocities within predefined bounds, producing a range of models that fit the observed data and quantify uncertainty and trade-offs, such as the correlation between Vs and layer thickness (Olafsdottir et al., 2020; Shapiro & Ritzwoller, 2002). The fast delta matrix algorithm by Buchen & Ben-Hador (1996) was used for forward dispersion modeling in MC inversion.

The starting model for the NLLS inversion was selected based on the overall dispersion trend and the low-high-low Vs structure reported by previous studies (Dou & Ajo-Franklin, 2014; Tourei et al., 2024a). In contrast, the parameter bounds for the MC inversion were defined using preliminary Vs results obtained from the NLLS solution to ensure physically realistic sampling. Combining the deterministic NLLS solution with the MC ensemble provides a more robust evaluation of model uncertainty and reduces ambiguity in the interpretation of the derived Vs profiles.

## 4 RESULTS AND DISCUSSION

Fig. 3 compares dispersion images computed for the propagating wavefields recorded during Event 2 on two segments of the fiber: 290 to 460 m (southwest), and 460 to 880 m (northeast). The dispersion image for the southwest part of the fiber shows no coherent surface-wave energy (Fig. 3b), whereas the recorded wavefield on the northeast part of the fiber exhibits clear and continuous energy between 5 Hz and 20 Hz (Fig. 3c), which was used for Vs inversion. A similar preferential direction effect was observed for Event 1, but in the opposite direction: the propagating wave recorded on the southwest portion of the fiber (blue double-headed arrow in Fig. 4a) displays clear moveout (Fig. 2b), whereas the northeast portion does not (additional details in Figure S3). These observations suggest that asymmetry in the coherence of observed wavefields on either side may be a combination of source radiation pattern and strong localized scattering effects due to heterogeneous ice distribution (Roy & Jakka, 2017; Steinel et al., 2014; Taipodia et al., 2019). Simple 2D elastic modeling of a source originating at the boundary of an ice wedge embedded in a layered permafrost medium suggests that one should expect differences on either side of the DAS array, as shown in the supplementary material (Text S3-5). Future 3D elastic-wave forward modeling and cryoseismic simulations, accounting for source mechanisms and material heterogeneity, can better quantify these source and wave propagation effects in permafrost environments.

The dispersion results for Event 2 (Fig. 3c), whose source was located at approximately the same distance along the fiber as Event 1 (Fig. 2a), show that phase velocity increases with frequency, indicating inverse dispersion behavior common in permafrost. In typical subsurface conditions, where soil stiffness increases with depth as a result of higher effective stress, the phase velocity generally decreases with frequency (normal dispersion). A similar behavior was observed in Fig. 2b, where phase velocity increased between 3-6 Hz, decreased near 10 Hz, and then increased again up to 18 Hz. These alternating dispersion trends likely reflect layered permafrost structure, where strong contrast in mechanical properties of ice-rich and ice-poor zones produces low-high-low Vs patterns observed in the previous permafrost studies in Utqiaġvik (e.g., Dou & Ajo-Franklin, 2014; Tourei et al., 2024a). This complex velocity distribution suggests that ice-

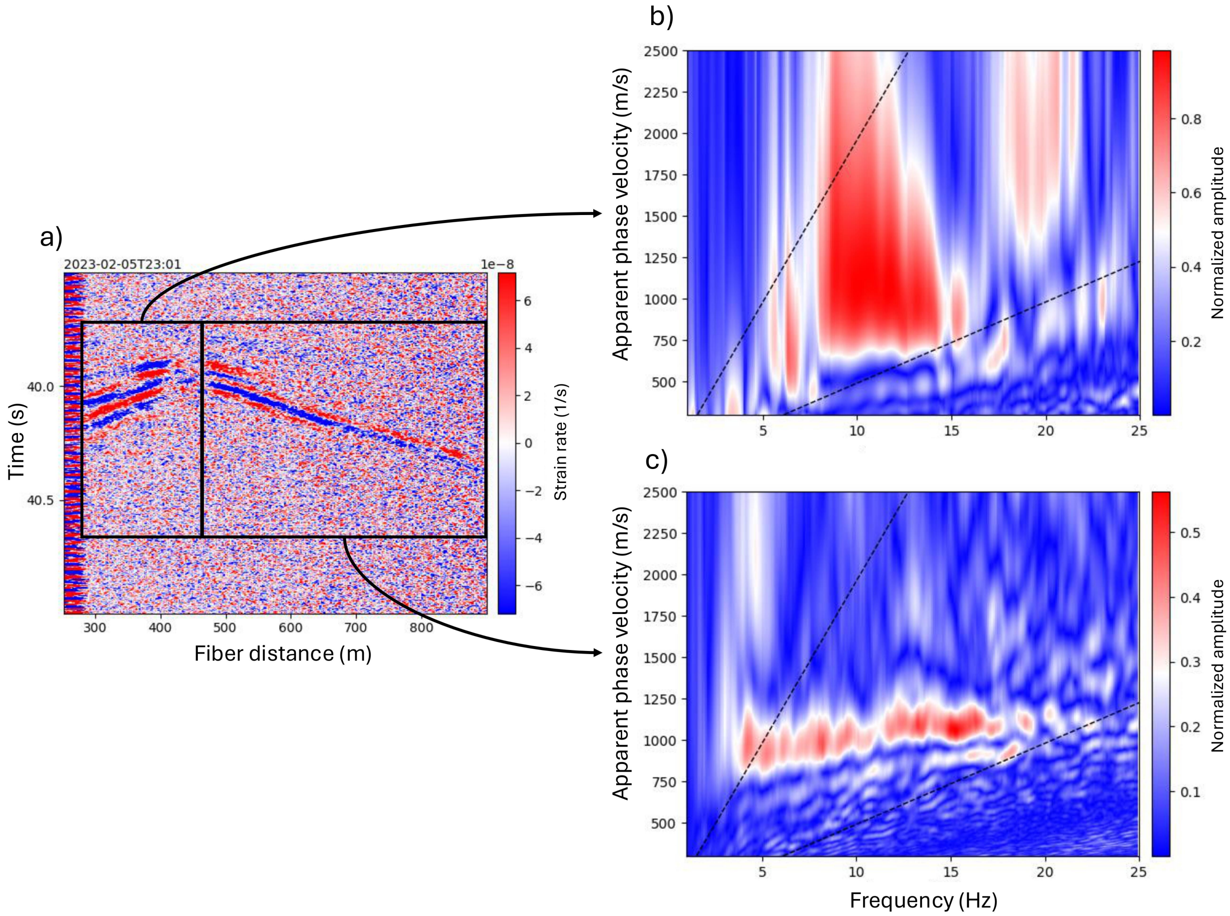


**Figure 3.** The raster plot (a) for cryoseismic Event 2 and the wave propagation effect on the dispersion results for the southwest (b) and northeast (c) segments of the fiber.

rich layers or frozen interbeds may be embedded within softer frozen soils, producing localized impedance contrasts that influence surface-wave propagation.

By inverting the dispersion curves derived from the phase-velocity–frequency images, we generated 1D Vs profiles from individual cryoseismic events. Fig. 4b presents two representative Vs profiles inverted from Events 1 and 2 on two different array segments (Fig. 4a), using the NLLS method with an L2-norm misfit between the theoretical and observed dispersion curves of 69 m/s and 61 m/s, respectively. We observe the low-high-low velocity structure in both Vs profiles. Due to the large spatial coverage provided by the DAS array and the low-frequency content of the recorded surface waves from these events, it was possible to invert for Vs down to depths of approximately 110 m and 82 m for Events 1 and 2, respectively. Such depth penetration would not be achievable using a conventional 24 m active-source survey line as discussed by (Tourei et al., 2024a). This extended depth sensitivity provides valuable subsurface information for geotechnical engineering applications, such as pile foundation design for high-rise infrastructure that requires characterization of deeper, load-bearing strata. It should be noted that although the array length for Event 2 (420 m) is greater than that of Event 1 (190 m), the maximum investigation depth for Event 1 is deeper. This is because the dispersion picks for Event 1 include lower-frequency components (starting around 3 Hz, as shown in Fig. 2b associated with higher phase velocities, which correspond to longer wavelengths and greater penetration depth.

As shown in Fig. 4a, the dispersion analyses were performed on array segments of approximately 320 m for Event 1 (Fig. 2a) and 420 m for Event 2 (Fig. 3a), both during winter 2023. Consequently, the resulting Vs models represent spatially averaged properties over those intervals. Despite this spatial averaging, the results reveal pronounced vertical and lateral heterogeneity and distinct high-velocity zones within the upper permafrost. As shown in Fig. 4, elevated Vs values occur between 47-88 m depth for Event 1 on the southwest segment of the fiber (noted in Fig. 4a and blue Vs profile in Fig. 4b). However, for Event 2 on the northeast segment of the fiber (green Vs profile in Fig. 4b), a similar high-velocity interval is observed between 13-42 m. In contrast, low-velocity zones are observed below 13 m and between 42–82 m on the northeast segment, and between 20-40 m on the southwest segment.

The high-velocity layers likely correspond to ice-rich zones, where increased ice bonding substantially enhances the stiffness and shear rigidity of the frozen soil matrix. The presence of a stiff layer is consistent with the occurrence of ice-cemented permafrost, overlying softer, partially frozen sediments (Lachenbruch, 1962; Loktev et al., 2012; Munroe et al., 2007; Tourei et al., 2024a). The low-velocity zones potentially reflect unfrozen saline layers, such as cryopeg features, that inhibit complete freezing. Similar low-velocity anomalies attributed to saline cryopegs have been reported previously in Utqiaġvik (Brown, 1969; Meyer et al., 2010; O'Sullivan et al., 1966; Overduin et al., 2012; Tourei et al., 2024a). Furthermore, the observation that the high-Vs layer on the southwest segment appears deeper than that on the northeast segment suggests a dipping geometry of the ice-rich permafrost horizon. This geometry could reflect spatial variability in ground-ice accumulation, differential freezing or thawing, or enhanced basal degradation near

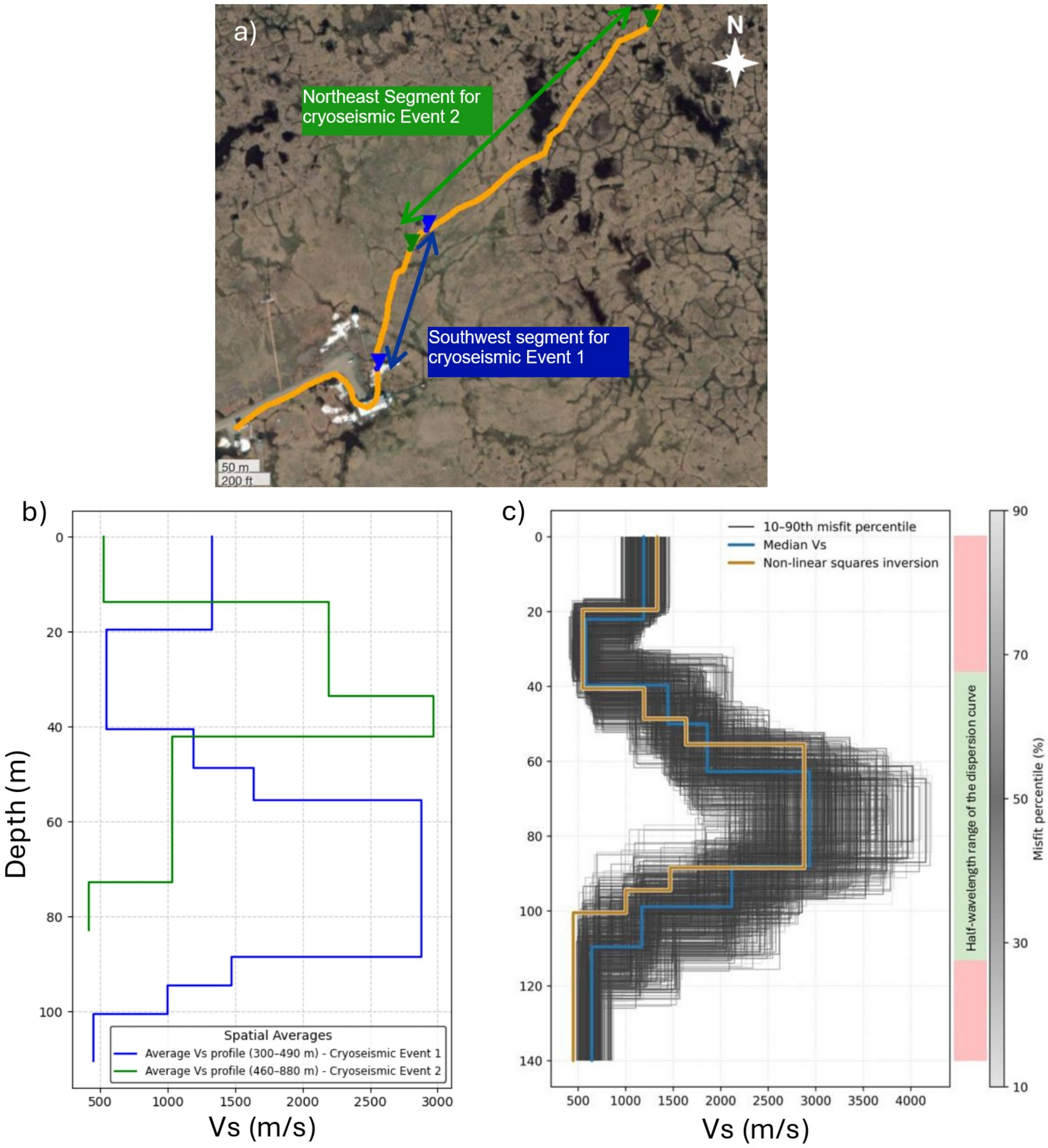


**Figure 4.** a) Enlarged view of the fiber segments used for MASW analysis; b) The corresponding inverted Vs profiles; and c) Ensemble of accepted MC Vs models for Event 1, shaded by misfit percentile (10–90; darkest at the median), overlaid with the median Vs (blue) and the NLLS solution (orange).

the coast, potentially associated with variability of surface water drainage direction towards the coastline or deeper saline-water intrusion. The available data do not allow these mechanisms to be distinguished. Our findings demonstrate the capability of fiber-based, multichannel near-surface techniques to capture distributed variations in permafrost structure over large spatial regions. Unlike conventional borehole or point-based geotechnical observations, DAS enables continuous, distributed measurements, offering a powerful framework for improving the resolution and spatial coverage of in-situ permafrost characterization.

It should also be noted that the obtained phase velocities represent apparent velocities, as the exact source-to-array orientation is approximate; therefore, deviations from an ideal in-line configuration can lead to a slight overestimation of phase velocity (Foti et al., 2018; Park et al., 1999). In this study, sources were selected with features suggesting an approximately in-line source orientation, supported by the close temporal alignment of body- and surface-wave arrivals (Fig. 2a). Nonetheless, although the depth-wise trend of the Vs profile is expected to remain consistent, potential azimuthal variations or lateral source offsets may have unrealistically increased the inverted Vs values, introducing minor uncertainties into the Vs profiles; this highlights the importance of event localization and azimuthal correction in future analyses.

Fig. 4c presents the ensemble of accepted Vs models from the MC inversion with misfit below 5%, colored by misfit percentile (10th–90th; darkest near the median) to convey posterior dispersion, together with the MC median profile and the NLLS solution for Event 1. The concentration of the model's percentile delineates depth intervals that are well constrained by the data (narrow, dark bands) versus poorly resolved sections (broad, pale spreads), reflecting the principal trade-offs between Vs and layer thickness in Rayleigh-wave inversion. The light green bar marks the depth range corresponding to approximately half a wavelength of the analyzed dispersion picks, whereas the light-red sections represent the fitted Vs profiles derived from the inversion, signifying regions of lower confidence and interpretational uncertainty. The NLLS model closely tracks the MC median, particularly at depths greater than 50 m, indicating that the deterministic optimum lies near the center of the posterior. Departures occur where the percentile spread widens, with the NLLS solution preferentially selecting one end of the admissible Vs-thickness manifold. These differences underscore the non-uniqueness of the inverse problem: the NLLS profile provides a single best-fit realization, whereas the MC percentile analysis quantifies the range of models that fit the data within tolerance, thereby offering a more complete characterization of parameter uncertainty and resolution.

Comparing the characterized high-Vs zone with the active-source MASW study in Utqiaġvik (Tourei et al., 2024a), the high-Vs zone in the present study appears at greater depths, primarily due to the lower source depth of the cryoseismic events and the use of longer array apertures. Furthermore, the limited high-frequency content in this dataset reduces our ability to resolve the upper 20–40 m with confidence. In contrast, the active-source survey achieved higher resolution in the shallow subsurface, benefiting from a shorter array geometry and a richer high-frequency wavefield. Joint interpretation of both surveys enables multiscale characterization of permafrost structure. The shallow ice-rich zones are associated with ice-wedge polygons and near-surface ice variability patterns, while the deeper high-velocity zones may reflect long-term climatic influences that facilitated the formation of persistent ice-rich layers, potentially accounting for the elevated Vs at depth.

Laboratory and field studies have reported Vs values up to 3,000 m/s in ice-cemented or ice-rich sandy permafrost (Ji et al., 2024; Young et al., 2022). Additionally, Shaw (1986) demonstrated that the elastic properties of ice vary substantially among crystalline phases depending on their formation temperature and pressure. These findings support our interpretation that the deeper, high-velocity layers identified in the inversions likely represent dense, ice-rich permafrost formed under low-temperature and high-confining-pressure conditions. Such conditions are consistent with long-term cold climate regimes and prolonged freezing periods, which may promote the accumulation and preservation of massive ground ice at depth.

## 5 CONCLUSIONS

Because passive DAS monitoring is non-destructive to permafrost and provides large spatial coverage with fine spatial resolution over long time periods, it shows promise for filling data gaps in remote areas to provide new knowledge about vulnerable permafrost structure. Naturally occurring cryoseismic events supply the seismic energy needed for near-surface imaging, and future research should investigate the repeatability of these signals and inversions to enable time-lapse monitoring in remote areas where active-source studies and ambient noise interferometry are impractical. By detecting these events and analyzing their surface-wave dispersion response, accounting for the effects of geometry and DAS gauge length, inversion of Vs profiles becomes possible. Depending on the frequency content and corresponding wavelengths, characterization to depths of up to 140 m can be achieved. Comparison between NLLS and MC inversions demonstrates that integrating deterministic and stochastic approaches improves the robustness and uncertainty assessment of the derived Vs models. Meanwhile, inversion uncertainties must be considered, and ground-truth validation through borehole or direct sampling is essential to improve confidence in the results. These findings highlight the importance of non-destructive, long-term in-situ monitoring methods that minimize disturbance to sensitive permafrost environments. This new combination of DAS recording passive cryoseismic events may drastically reduce the cost of repeated field mobilization in Arctic regions where geotechnical engineers require mechanical property maps of thaw-susceptible permafrost to improve infrastructure resilience, making this approach a promising technique that is worth further investigation and practical refinement by both geophysicists and engineers.

## ACKNOWLEDGMENTS

This study was supported by NSF under CMMI-2034363, CMMI-2034366, CMMI-2034380, and CISE-2227018. We acknowledge the support and facilities provided by UIC Science, NOAA, and the ARM Climate Research Facility of the DOE. We thank John A. Hole, Derrick J.A. Chambers, and Xiaohang Ji for valuable discussions and support. We thank Min Liew, Nolan Roth, Anne Jensen, Dmitry Nicolsky, Matthew Hallissey, and Chris McComb for their field support.

## DATA AVAILABILITY

The das-anomaly Python package (Tourei, 2026a) was used for cryoseismic event detection. DAS-Core (Chambers et al., 2024) was used for DAS dispersion analysis, along with hvsrpy (Vantassel, 2025) and SWinvert (Vantassel & Cox, 2021) packages for post-processing of the dispersion images. MasavesPy library (Olafsdottir et al., 2024) was used for MC inversion, and Intelligent-MASW (Liu et al., 2020) was used for NLLS inversion of the Vs profiles. The DAS data are available on Arctic Data Center (Tourei, 2026b) and A21K data are reported through EARTHSCOPE DMC and were accessed using ObsPy IRIS client (Beyreuther et al., 2010).

## References

Afonin, N., Kozlovskaya, E., Moisio, K., Kokko, E. R., & Okkonen, J., 2024. Frost quakes in wetlands in northern Finland during extreme winter weather conditions and related hazard to urban infrastructure, *Cryosphere*, **18**(5), 2223–2238, doi: 10.5194/TC-18-2223-2024.

Akhtarshenas, S., Asce, S. M., Abdelaziz, S. L., & Asce, A. M., 2024. Dynamic Properties of Frozen Soils: A Literature Review and Future Research Needs, pp. 421–431, doi: 10.1061/9780784485408.042.

Babaee, A., Bradshaw, A. S., & Baxter, C. D., 2025. Relationship between shear band dilation and stress-corrected relative density under constant normal stiffness (CNS) conditions, *Ocean Engineering*, **339**, 122078, doi: 10.1016/j.oceaneng.2025.122078.

Barosh, P. J., 2000. Frostquakes in New England, *Engineering Geology*, **56**(3-4), 389–394, doi: 10.1016/S0013-7952(99)00092-7.

Beyreuther, M., Barsch, R., Krischer, L., Megies, T., Behr, Y., & Wassermann, J., 2010. ObsPy: A Python Toolbox for Seismology, *Seismological Research Letters*, **81**(3), 530–533, doi: 10.1785/GSSRL.81.3.530.

Brown, J., 1969. *Ionic Concentration Gradients in Permafrost Barrow, Alaska, Cold Regions Research and Engineering Laboratory, Corps of Engineers*, US Army, Hanover, New Hampshire.

Buchen, P. W. & Ben-Hador, R., 1996. Free-mode surface-wave computations, *Geophysical Journal International*, **124**(3), 869–887, doi: 10.1111/j.1365-246X.1996.tb05642.x.

Castongia, E., Wang, H. F., Lord, N., Fratta, D., Mondanos, M., & Chalari, A., 2017. An Experimental Investigation of Distributed Acoustic Sensing (DAS) on Lake Ice, *Journal of Environmental and Engineering Geophysics*, **22**(2), 167–176, doi: 10.2113/JEEG22.2.167.

Chambers, D., Jin, G., Tourei, A., Issah, A. H. S., Lellouch, A., Martin, E. R., Zhu, D., Girard, A. J., Yuan, S., Cullison, T., Snyder, T., Kim, S., Danes, N., Punithan, N., Boltz, M. S., & Mendoza, M. M., 2024. DASCore: a Python Library for Distributed Fiber Optic Sensing, *Seismica*, **3**(2), 10.26443/seismica.v3i2.1184, doi: 10.26443/SEISMICA.V3I2.1184.

Cheng, F., Lindsey, N. J., Sobolevskaia, V., Dou, S., Freifeld, B., Wood, T., James, S. R., Wagner, A. M., & Ajo-Franklin, J. B., 2022. Watching the Cryosphere Thaw: Seismic Monitoring of Permafrost Degradation Using Distributed Acoustic Sensing During a Controlled Heating Experiment, *Geophysical Research Letters*, **49**(10), e2021GL097195, doi: 10.1029/2021GL097195.

Cheng, T., Cox, B. R., Vantassel, J. P., & Manuel, L., 2020. A statistical approach to account for azimuthal variability in single-station HVSR measurements, *Geophysical Journal International*, **223**(2), 1040–1053, doi: 10.1093/GJI/GGAA342.

Dangwal, D., Behm, M., Chen, X., & Soreghan, G. S., 2023. Imaging an Enigmatic Paleovalley with Passive Seismic Methods (Unaweep Canyon, Colorado, United States), *The Seismic Record*, **3**(2), 116–124, doi: 10.1785/0320220048.

Dou, S. & Ajo-Franklin, J. B., 2014. Full-wavefield inversion of surface waves for mapping embedded low-velocity zones in permafrost, *Geophysics*, **79**(6), EN107–EN124, doi: 10.1190/geo2013-0427.1.

Dou, S., Lindsey, N., Wagner, A. M., Daley, T. M., Freifeld, B., Robertson, M., Peterson, J., Ulrich, C., Martin, E. R., & Ajo-Franklin, J. B., 2017. Distributed Acoustic Sensing for Seismic Monitoring of the Near Surface: A Traffic-Noise Interferometry Case Study, *Scientific Reports*, **7**(1), 1–12, doi: 10.1038/s41598-017-11986-4.

Fang, J., Yang, Y., Shen, Z., Biondi, E., Wang, X., Williams, E. F., Becker, M. W., Eslamian, D., Zhan, Z., Yang, Y., Shen, Z., Biondi, E., Wang, X., Williams, E. F., Becker, M. W., Eslamian, D., & Zhan, Z., 2023. Directional Sensitivity of DAS and Its Effect on Rayleigh-Wave Tomography: A Case Study in Oxnard, California, *Seismological Research Letters*, **94**(2A), 887–897, doi: 10.1785/0220220235.

Foti, S., Hollender, F., Garofalo, F., Albarello, D., Asten, M., Bard, P. Y., Comina, C., Cornou, C., Cox, B., Di Giulio, G., Forbriger, T., Hayashi, K., Lunedei, E., Martin, A., Mercerat, D., Ohrnberger, M., Poggi, V., Renalier, F., Sicilia, D., & Socco, V., 2018. Guidelines for the good practice of surface wave analysis: a product of the InterPACIFIC project, *Bulletin of Earthquake*

*Engineering*, **16**(6), 2367–2420, doi: 10.1007/S10518-017-0206-7/FIGURES/34.

Gribler, G., Liberty, L. M., Mikesell, T. D., & Michaels, P., 2016. Isolating retrograde and prograde Rayleigh-wave modes using a polarity mute, *https://doi.org/10.1190/geo2015-0683.1*, **81**(5), V379–V385, doi: 10.1190/GEO2015-0683.1.

Harmon, N., Rychert, C. A., Davis, J., Brambilla, G., Buffet, W., Chichester, B., Dai, Y., Bogiatzis, P., Snook, J., van Putten, L., & Masoudi, A., 2022. Surface deployment of DAS systems: Coupling strategies and comparisons to geophone data, *Near Surface Geophysics*, **20**(5), 465–477, doi: 10.1002/NSG.12232.

Hjort, J., Streletskiy, D., Doré, G., Wu, Q., Bjella, K., & Luoto, M., 2022. Impacts of permafrost degradation on infrastructure, *Nature Reviews Earth and Environment*, **3**(1), doi: 10.1038/s43017-021-00247-8.

Ji, X., Asce, S. M., Xiao, M., Asce, F., Martin, E. R., & Zhu, T., 2024. Statistical Evaluation of Seismic Velocity Models of Permafrost, *Journal of Cold Regions Engineering*, **38**(3), 04024021, doi: 10.1061/JCRGEI.CRENG-760.

Jorgenson, M. T., Yoshikawa, K., Kanevskiy, M., Shur, Y., Romanovsky, V., Marchenko, S., & Jones, B., 2008. Permafrost characteristics of Alaska, in *Proceedings of the ninth international conference on permafrost*, vol. 3, pp. 121–122, University of Alaska.

Kausel, E. & Roësset, J. M., 1981. Stiffness matrices for layered soils, *Bulletin of the Seismological Society of America*, **71**(6), 1743–1761, doi: 10.1785/bssa0710061743.

Lachenbruch, A. H., 1962. Mechanics of thermal contraction cracks and ice-wedge polygons in permafrost, p. 69.

Lehujeur, M., Chevrot, S., Villaseñor, A., Masini, E., Saspiturry, N., Lescoutre, R., & Sylvander, M., 2021. Three-dimensional shear velocity structure of the Mauléon and Arzacq Basins (Western Pyrenees), *Bulletin de la Société Géologique de France*, **192**(1), 47, doi: 10.1051/BSGF/2021039.

Leung, A. C. W., Gough, W. A., & Shi, Y., 2017. Identifying Frostquakes in Central Canada and Neighbouring Regions in the United States with Social Media, pp. 201–222, doi: 10.1007/978-3-319-51629-5_9.

Liu, H., Maghoul, P., & Shalaby, A., 2020. Intelligent MASW, doi: 10.5281/ZENODO.3776875.

Loktev, A., Bondarev, V., Kulikov, S., & Rokos, S., 2012. Russian Arctic Offshore Permafrost.

Lomax, A. & Snieder, R., 1994. Finding sets of acceptable solutions with a genetic algorithm with application to surface wave group dispersion in Europe, *Geophysical Research Letters*, **21**(24), 2617–2620, doi: 10.1029/94GL02635.

Luo, B., Jin, G., & Stanek, F., 2021. Near-field strain in distributed acoustic sensing-based microseismic observation, *https://doi.org/10.1190/geo2021-0031.1*, **86**(5), P49–P60, doi: 10.1190/GEO2021-0031.1.

Macquet, M., Paul, A., Pedersen, H. A., Villaseñor, A., Chevrot, S., Sylvander, M., & Wolyniec, D., 2014. Ambient noise tomography of the Pyrenees and the surrounding regions: inversion for a 3-D Vs model in the presence of a very heterogeneous crust, *Geophysical Journal International*, **199**(1), 402–415, doi: 10.1093/GJI/GGU270.

Maraschini, M. & Foti, S., 2010. A Monte Carlo multimodal inversion of surface waves, *Geophysical Journal International*, **182**(3), 1557–1566, doi: 10.1111/J.1365-246X.2010.04703.X.

Martin, E., 2021. Introduction to Distributed Acoustic Sensing.

Meyer, H., Schirrmeister, L., Andreev, A., Wagner, D., Hubberten, H. W., Yoshikawa, K., Bobrov, A., Wetterich, S., Opel, T., Kandiano, E., & Brown, J., 2010. Lateglacial and Holocene isotopic and environmental history of northern coastal Alaska – Results from a buried ice-wedge system at Barrow, *Quaternary Science Reviews*, **29**(27-28), 3720–3735, doi: 10.1016/J.QUASCIREV.2010.08.005.

Mordret, A., Landés, M., Shapiro, N. M., Singh, S. C., & Roux, P., 2014. Ambient noise surface wave tomography to determine the shallow shear velocity structure at Valhall: depth inversion with a Neighbourhood Algorithm, *Geophysical Journal International*, **198**(3), 1514–1525, doi: 10.1093/GJI/GGU217.

Munroe, J. S., Doolittle, J. A., Kanevskiy, M. Z., Hinkel, K. M., Nelson, F. E., Jones, B. M., Shur, Y., & Kimble, J. M., 2007. Application of ground-penetrating radar imagery for three-dimensional visualisation of near-surface structures in ice-rich permafrost, Barrow, Alaska, *Permafrost and Periglacial Processes*, **18**(4), 309–321, doi: 10.1002/PPP.594.

Nikonov, A. A., 2010. Frost quakes as a particular class of seismic events: Observations within the East-European platform, *Izvestiya, Physics of the Solid Earth*, **46**(3), 257–273, doi: 10.1134/S1069351310030079/METRICS.

Okkonen, J., Neupauer, R. M., Kozlovskaya, E., Afonin, N., Moisio, K., Taewook, K., & Muurinen, E., 2020. Frost Quakes: Crack Formation by Thermal Stress, *Journal of Geophysical Research: Earth Surface*, **125**(9), e2020JF005616, doi: 10.1029/2020JF005616.

Olafsdottir, E. A., Erlingsson, S., & Bessason, B., 2020. Open-Source MASW Inversion Tool Aimed at Shear Wave Velocity Profiling for Soil Site Explorations, *Geosciences 2020, Vol. 10, Page 322*, **10**(8), 322, doi: 10.3390/GEOSCIENCES10080322.

Olafsdottir, E. A., Bessason, B., Erlingsson, S., Kaynia, A. M., Olafsdottir, E. A., Bessason, B., Erlingsson, S., & Kaynia, A. M., 2024. A Tool for Processing and Inversion of MASW Data and a Study of Inter-session Variability of MASW, *Geotechnical Testing Journal* , **47**(5), 1006–1025, doi: 10.1520/GTJ20230380.

O'Sullivan, J. B., P., P., Westermann, S., Yoshikawa, K., Haberlau, T., Romanovsky, V., & Wetterich, S., 1966. Geochemistry of permafrost, Barrow, Alaska, *Permafrost International Conference*, **117**, 30–37, doi: 10.1029/2011JF002088.

Overduin, P. P., Westermann, S., Yoshikawa, K., Haberlau, T., Romanovsky, V., & Wetterich, S., 2012. Geoelectric observations of the degradation of nearshore submarine permafrost at Barrow (Alaskan Beaufort Sea), *Journal of Geophysical Research: Earth Surface*, **117**(F2), 2004, doi: 10.1029/2011JF002088.

Park, C. B., Miller, R. D., Xia, J., & Survey, K. G., 1998. Imaging dispersion curves of surface waves on multi-channel record, in *SEG Technical Program Expanded Abstracts*.

Park, C. B., Miller, R. D., & Xia, J., 1999. Multimodal Analysis of High Frequency Surface Waves, in *Symposium on the Application of Geophysics to Engineering and Environmental Problems 1999*, Symposium on the Application of Geophysics to Engineering and Environmental Problems Proceedings, pp. 115–121, Environment and Engineering Geophysical Society, doi: doi:10.4133/1.2922596.

Rocha dos Santos, G. & Zhu, T., 2025a. Distributed Sensing of Ice-Wedge Cracking in Utqiaġvik,

*Distributed Acoustic Sensing Recordings of Cryoseismicity Enable Seismic Imaging of Permafrost in Remote Ar*
Alaska, *AGU*, (1673), NS33C–1673.

Rocha dos Santos, G. & Zhu, T., 2025b. Seismic Tremors From Sea-Landfast Ice Interactions Near Utqiaġvik, Alaska, *Geophysical Research Letters*, **52**(15), e2025GL117458, doi: 10.1029/2025GL117458.

Rodríguez Tribaldos, V. & Ajo-Franklin, J. B., 2021. Aquifer Monitoring Using Ambient Seismic Noise Recorded With Distributed Acoustic Sensing (DAS) Deployed on Dark Fiber, *Journal of Geophysical Research: Solid Earth*, **126**(4), doi: 10.1029/2020JB021004.

Romeyn, R., Hanssen, A., Ole Ruud, B., Meling Stemland, H., & Arne Johansen, T., 2021. Passive seismic recording of cryoseisms in Adventdalen, Svalbard, *Cryosphere*, **15**(1), 283–302, doi: 10.5194/TC-15-283-2021.

Romeyn, R., Hanssen, A., & Kohler, A., 2022. Long-term analysis of cryoseismic events and associated ground thermal stress in Adventdalen, Svalbard, *Cryosphere*, **16**(5), 2025–2050, doi: 10.5194/TC-16-2025-2022.

Roy, N. & Jakka, R. S., 2017. Near-field effects on site characterization using MASW technique, *Soil Dynamics and Earthquake Engineering*, **97**, 289–303, doi: 10.1016/J.SOILDYN.2017.02.011.

Shapiro, N. M. & Ritzwoller, M. H., 2002. Monte-Carlo inversion for a global shear-velocity model of the crust and upper mantle, *Geophysical Journal International*, **151**(1), 88–105, doi: 10.1046/J.1365-246X.2002.01742.X.

Shapiro, N. M., Singh, S. K., Almora, D., & Ayala, M., 2001. Evidence of the dominance of higher-mode surface waves in the lake-bed zone of the Valley of Mexico, *Geophysical Journal International*, **147**(3), 517–527, doi: 10.1046/J.0956-540X.2001.01508.X.

Shaw, G. H., 1986. Elastic properties and equation of state of high pressure ice, *The Journal of Chemical Physics*, **84**(10), 5862–5868, doi: 10.1063/1.449897.

Socco, L. V. & Strobbia, C., 2004. Surface-wave method for near-surface characterization: A tutorial, *Near surface geophysics*, **2**(4), 165–185.

Steinel, H., Hausmann, J., Werban, U., & Dietrich, P., 2014. Reliability of MASW profiling in near-surface applications, *Near Surface Geophysics*, **12**(6), 731–737, doi: 10.3997/1873-

0604.2014029.

Sun, H., Cheng, F., Xia, J., Guan, J., Li, Z., & Ajo-Franklin, J. B., 2025. Unveiling Cryosphere Dynamics by Distributed Acoustic Sensing and Data-Driven Hydro-Thermo Coupled Simulation, *Geophysical Research Letters*, **52**(2), e2024GL111188, doi: 10.1029/2024GL111188.

Taipodia, J., Baglari, D., & Dey, A., 2019. Effect of Source Characteristics on the Resolution of Dispersion Image from Active MASW Survey, *Indian Geotechnical Journal*, **49**(3), 314–327, doi: 10.1007/S40098-018-0335-1/METRICS.

Tourei, A., 2026a. DASDAE/das-anomaly: v0.0.8, doi: 10.5281/zenodo.12747212.

Tourei, A., 2026b. Seismic Events Recorded by A Distributed Acoustic Sensing Array Near Utqiaġvik, Alaska (2022-2023), doi: 10.18739/A2CN6Z21C.

Tourei, A., Ji, X., Rocha dos Santos, G., Czarny, R., Rybakov, S., Wang, Z., Hallissey, M., Martin, E. R., Xiao, M., Zhu, T., Nicolsky, D., & Jensen, A., 2024a. Mapping Permafrost Variability and Degradation Using Seismic Surface Waves, Electrical Resistivity, and Temperature Sensing: A Case Study in Arctic Alaska, *Journal of Geophysical Research: Earth Surface*, **129**(3), e2023JF007352, doi: 10.1029/2023JF007352.

Tourei, A., Martin, E. R., Ankamah, A. T., Hole, J. A., & Chambers, D. J., 2024b. An Autoencoder-Based Deep Learning Model for Enhancing Noise Characterization and Microseismic Event Detection in Underground Longwall Coal Mines Using Distributed Acoustic Sensing Monitoring, *58th US Rock Mechanics / Geomechanics Symposium 2024, ARMA 2024*, doi: 10.56952/ARMA-2024-0207.

Vantassel, J. P., 2025. hvsrpy: An Open-Source Python Package for Microtremor and Earthquake Horizontal-to-Vertical Spectral Ratio Processing, *Seismological Research Letters*, **96**(4), 2671–2682, doi: 10.1785/0220240395.

Vantassel, J. P. & Cox, B. R., 2021. SWinvert: a workflow for performing rigorous 1-D surface wave inversions, *Geophysical Journal International*, **224**(2), 1141–1156, doi: 10.1093/GJI/GGAA426.

Vantassel, J. P., Cox, B. R., Hubbard, P. G., & Yust, M., 2022. Extracting high-resolution, multi-mode surface wave dispersion data from distributed acoustic sensing measurements using the multichannel analysis of surface waves, *Journal of Applied Geophysics*, **205**, doi: 10.1016/j.jappgeo.2022.104776.

Viens, L., Perton, M., Spica, Z. J., Nishida, K., Yamada, T., & Shinohara, M., 2022. Understanding surface wave modal content for high-resolution imaging of submarine sediments with distributed acoustic sensing, *Geophysical Journal International*, **232**(3), 1668–1683, doi: 10.1093/GJI/GGAC420.

Wagner, A. M., Lindsey, N. J., Dou, S., Gelvin, A., Saari, S., Williams, C., Ekblaw, I., Ulrich, C., Borglin, S., Morales, A., & Ajo-Franklin, J., 2018. Permafrost Degradation and Subsidence Observations during a Controlled Warming Experiment, *Scientific Reports*, **8**(1), 1–9, doi: 10.1038/s41598-018-29292-y.

Wang, Z., Sun, C., & Wu, D., 2022. Multiscale linearized inversion of surface-wave dispersion curves, *Geophysical Prospecting*, **70**(1), 19–34, doi: 10.1111/1365-2478.13149/CITE/REFWORKS.

Wapenaar, K., Draganov, D., Snieder, R., Campman, X., & Verdel, A., 2010. Tutorial on seismic interferometry: Part 1 - Basic principles and applications, *Geophysics*, **75**(5), doi: 10.1190/1.3457445.

Wu, Y., Nakagawa, S., Kneafsey, T. J., Dafflon, B., & Hubbard, S., 2017. Electrical and seismic response of saline permafrost soil during freeze - Thaw transition, *Journal of Applied Geophysics*, **146**, 16–26, doi: 10.1016/J.JAPPGEO.2017.08.008.

Xia, J., Miller, R. D., & Park, C. B., 1999. Configuration of Near-Surface Shear-Wave Velocity by Inverting Surface Wave, in *Symposium on the Application of Geophysics to Engineering and Environmental Problems 1999*, Symposium on the Application of Geophysics to Engineering and Environmental Problems Proceedings, pp. 95–104, Environment and Engineering Geophysical Society, doi: doi:10.4133/1.2922698.

Young, C., Shragge, J., Schultz, W., Haines, S., Oren, C., Simmons, J., & Collett, T. S., 2022. Advanced Distributed Acoustic Sensing Vertical Seismic Profile Imaging of an Alaska North Slope Gas Hydrate Field, *Energy & Fuels*, **36**(7), 3481–3495, doi: 10.1021/ACS.ENERGYFUELS.1C04102.

Yuan, S. & Martin, E., 2025. Potential higher-mode bias in DAS-based MASW for near-surface characterization, Tech. rep., Center for Wave Phenomena.

## APPENDIX A: FOR EDITORS

This paper has been produced using the Blackwell Scientific Publications GJI LaTeX2e class file.

Supplementary Material (Online)

# Distributed Acoustic Sensing Recordings of Cryoseismicity Enable Permafrost Characterization in Remote Arctic Regions

Ahmad Tourei[1,2*], Eileen R. Martin[1,2], Gabriel Rocha dos Santos[3], Tieyuan Zhu[3], Nikhil Punithan[2], Ming Xiao[4]

(1) Hydrologic Science and Engineering Program, Colorado School of Mines, Golden, CO, USA

(2) Department of Geophysics, Colorado School of Mines, Golden, CO, USA

(3) Department of Geosciences, Pennsylvania State University, University Park, PA, USA

(4) Department of Civil and Environmental Engineering, Pennsylvania State University, University Park, PA, USA

## Contents of this file:



## Introduction

This document provides supporting information on:

- An example of a cryoseismic event with higher-order surface wave modes
- An overview of horizontal-to-vertical spectral ratio (HVSR) analysis performed for characterizing modal behavior of cryoseismic Event 1
- Dispersion analysis of the northeast fiber segment for cryoseismic Event 1
- Preliminary 2D numerical modeling for wave propagation effects on distributed acoustic sensing response

### Text S1.

Horizontal distributed acoustic sensing (DAS) arrays are inherently more sensitive to Rayleigh wave components with strong horizontal motion (i.e., large ellipticity), which can enhance the detection of higher-order modes that exhibit greater ellipticity than the fundamental mode (Fang et al., 2023; Shapiro et al., 2001; Viens et al., 2022). For a few cryoseismic events, the presence of higher-order modes was evident. For example, Figure S1 illustrates an example cryoseismic event, where both the fundamental and first higher-order Rayleigh modes are clearly identified. In contrast, higher-order modes were not initially observed for Cryoseismic Event 1 (Figure 2a-b) or Event 2 (Figure 3).

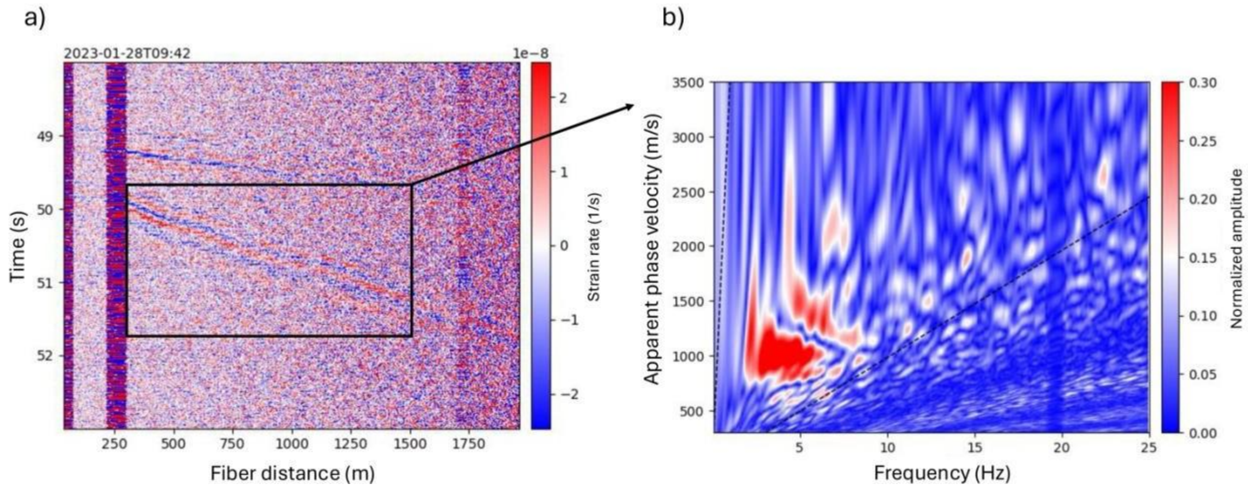


**Figure S1.** The time-domain raster plot (a) and the dispersion image with fundamental and first-order mode Rayleigh wave (b) for an example cryoseismic event.

**Text S2.**

As a complementary assessment of Rayleigh-wave modal content for Event 1, we performed horizontal-to-vertical spectral ratio (HVSR) analysis on the 3C seismometer data using a statistical approach to account for azimuthal variability (Cheng et al., 2020; Vantassel, 2025). As illustrated in Figure 4, results showed HVSR values exceeding unity above 11 Hz (observed as a separate moveout in Figure 2b), suggesting increased ellipticity at higher frequencies. Consequently, frequencies above 11 Hz were excluded from the inversion to ensure that only fundamental-mode Rayleigh-wave energy was considered. The absence of a prominent HVSR peak below 10 Hz suggests that the ellipticity for this event is relatively small, and thereby, the fundamental-mode Rayleigh response should be considered for DAS-based analysis and inversion. The HVSR results for Event 2 were noisier and exhibited greater fluctuation but remained mostly below 1, also supporting a fundamental-mode Rayleigh-wave interpretation. Additionally, the preliminary numerical modeling results provided below (S3-5) that the discontinuity of dispersion around 10 Hz (Figure 2b) is potentially due to strong scattering and mode conversion caused by the ice-wedge or ice-rich layer heterogeneity, where impedance contrasts between frozen and unfrozen layers disrupt the continuity of the Rayleigh-wave fundamental mode and lead to partial energy redistribution into higher modes.

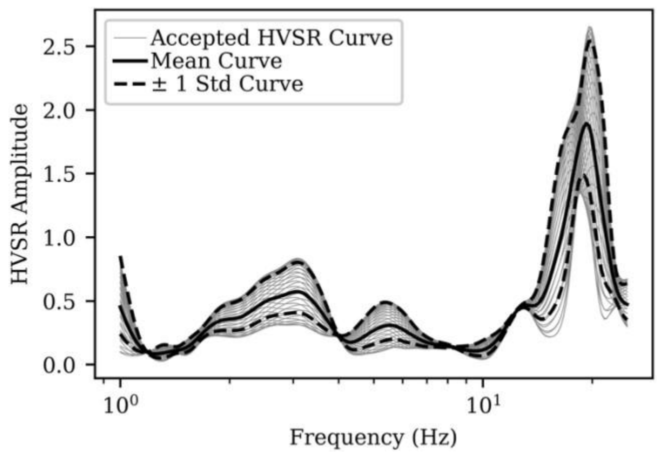


**Figure S2.** The HVSR curves from the 3-C seismometer for Cryoseismic Event 1

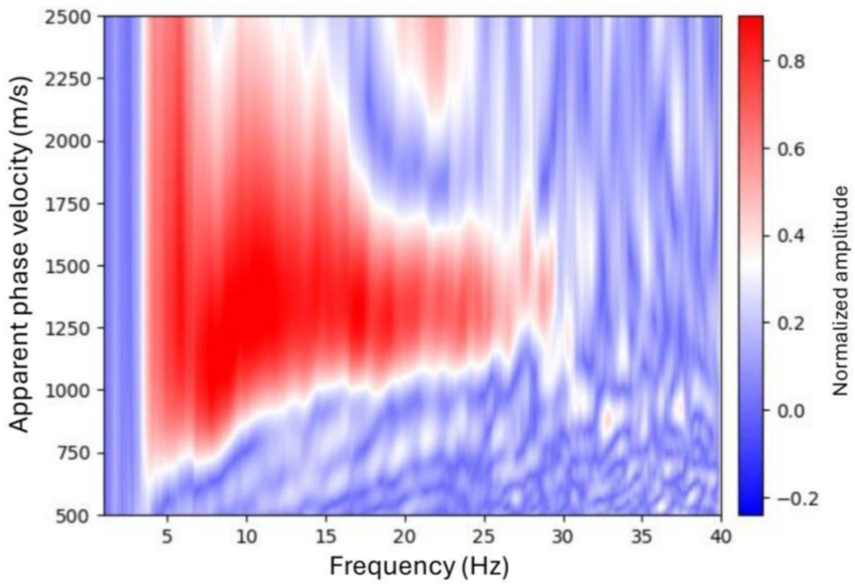


**Figure S3.** The wave propagation effect on the dispersion results for the northeast segment of the fiber in cryoseismic Event 1

**Text S3.**

**Numerical Array Geometry and Elastic Model**

A 2-D P-SV elastic plane-strain domain with Lx=Lz=500 m and Δx=Δz=1 m (501×501 nodes) was modeled. The P-SV supports P- (compressional) and SV-waves (vertically polarized shear waves), but not SH-waves (horizontally polarized shear waves). The Devito finite-difference framework (Luporini et al., 2020) was employed and customized for elastic wave modeling.

Stratigraphy of 5 layers as shown in Figure S4 (Vp in km/s; Vs is assumed to be Vp/1.6):

- 0–2 m: 0.5
- 2–22 m: 1.5
- 22–142 m: 4.5
- 142–192 m: 2.5
- 192-500 m: 1.5

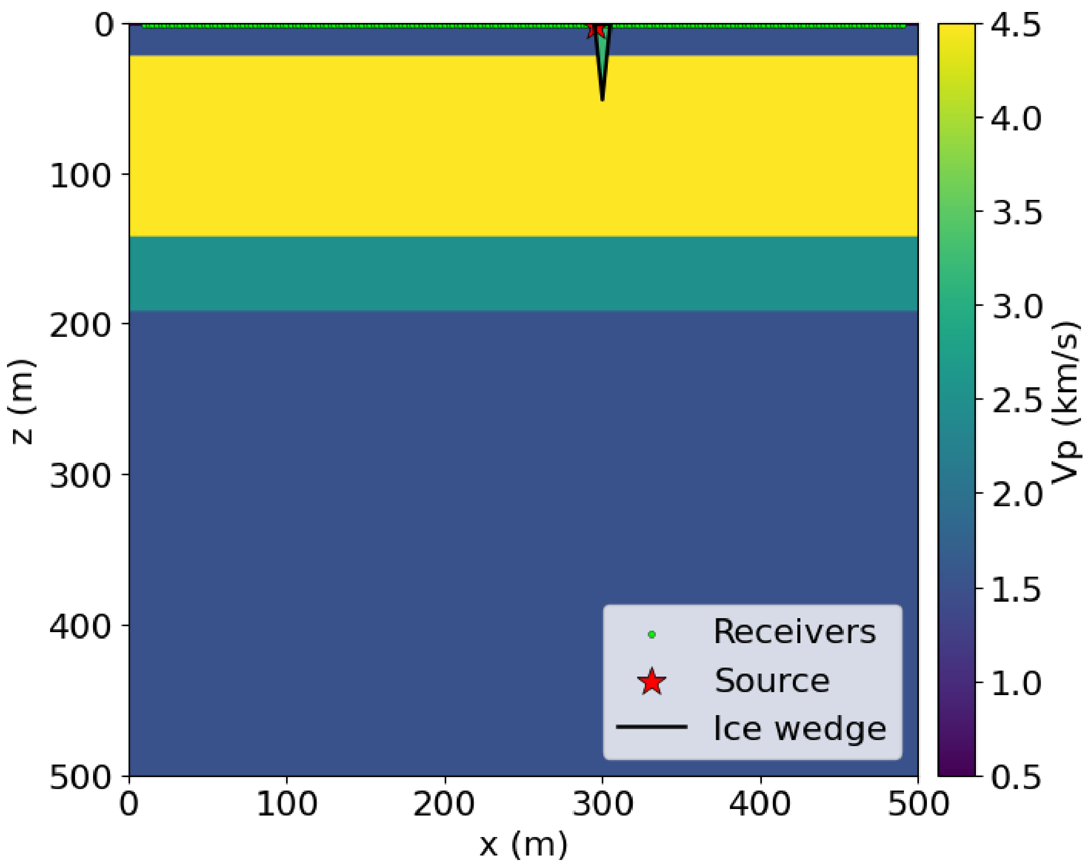


**Figure S4.** Geometry of the elastic model.

The model parameters and boundary conditions are as follows:

- Mass density: 2000 kg/m³ everywhere except for the top 2 m with 1500 kg/m³
- Ice wedge: A triangular inclusion centered at x=300 m, top at z=1 m, 10 m base width and 50 m height; ice properties assigned inside the triangle.
- Source: Ricker wavelet, f0=10 Hz, implemented as an explosive (isotropic) stress source by injecting into $\tau_{xx}$ and $\tau_{zz}$. The source is placed just beneath the free surface; at xs=296 m and zs=2 m (at the left side of the ice-wedge)

- Receivers: A horizontal line at z=1 m with 2.5 m spacing. With the sponge margin, the active aperture is ~10–490 m. We record the horizontal particle velocity vx(t,x).
- Boundary conditions: Traction-free at the top; quadratic sponge on the left, right, and bottom boundaries (thickness nbl=10 grid points, strength factor α=3) added to both velocity and stress updates to suppress side/bottom reflections.
- Time stepping: CFL-limited Δt (0.45 Courant factor for 2-D), total record length up to 2 s; plots in the figure focus on the early portion.

**Text S4.**

## Strain-Rate Preprocessing

The first preprocessing step converts cumulative velocity to strain rate. Assuming a homogeneous isotropic medium and wavelengths at least twice the interrogator gauge length ($l$), the DAS-measured strain rate ($\dot{\varepsilon}$) can be expressed as the finite difference of fiber-aligned particle velocities ($\dot{u}$) recorded by two hypothetical horizontal geophones separated by $l$. Equation 1 was used for this conversion, allowing flexible selection of the effective gauge length during processing.

$$\dot{\varepsilon}(x,t) = \frac{\dot{u}(x + l/2\,, t) - \dot{u}(x - l/2\,, t)}{l} \tag{1}$$

Figure S5 shows the shot gather horizontal particle velocity response in the time domain.

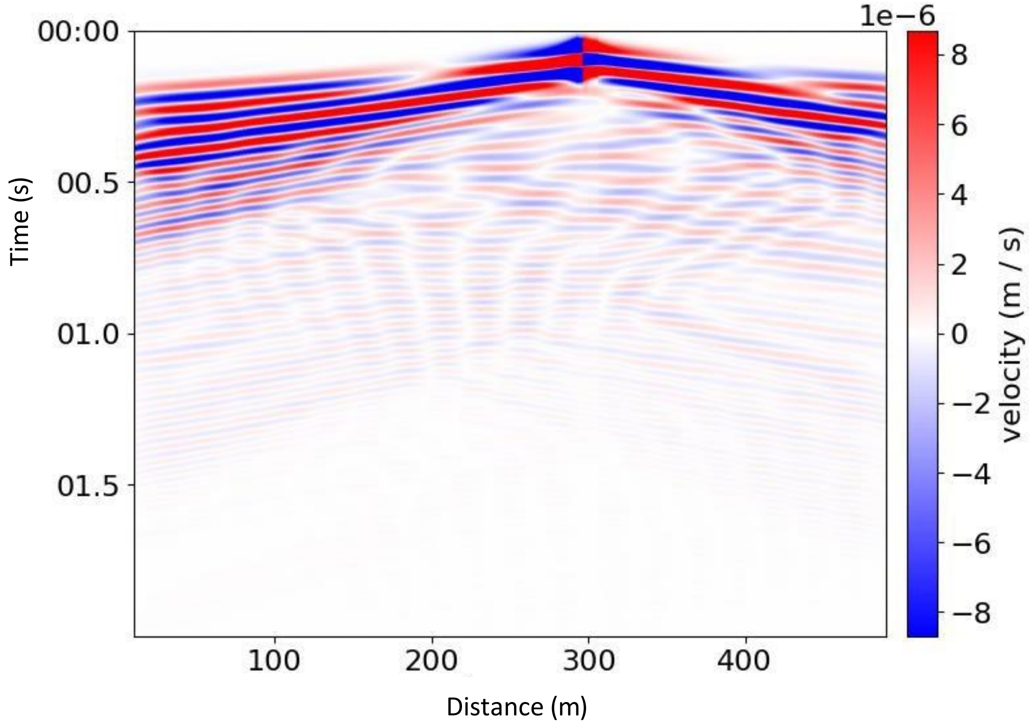


**Figure S5.** Raster plot of the horizontal particle velocity response of the array.

To emphasize the DAS response for a horizontal array, we use Equation 1 to convert particle velocity to strain rate by a finite difference along the array with a gauge length of 5 m. That is a central difference over the gauge length using every other receiver (receiver spacing = 2.5 m, therefore step of two channels). Edges are discarded after differencing.

As illustrated in Figure S6, a strong Rayleigh wavefield propagates away from the source on both sides of the ice-wedge (dominant energy just beneath the surface). Also, later arrivals with higher apparent velocities correspond to deeper reverberations and converted modes are observed. A local amplitude notch near x≈300 m corresponds to scattering and mode conversion at the ice wedge.

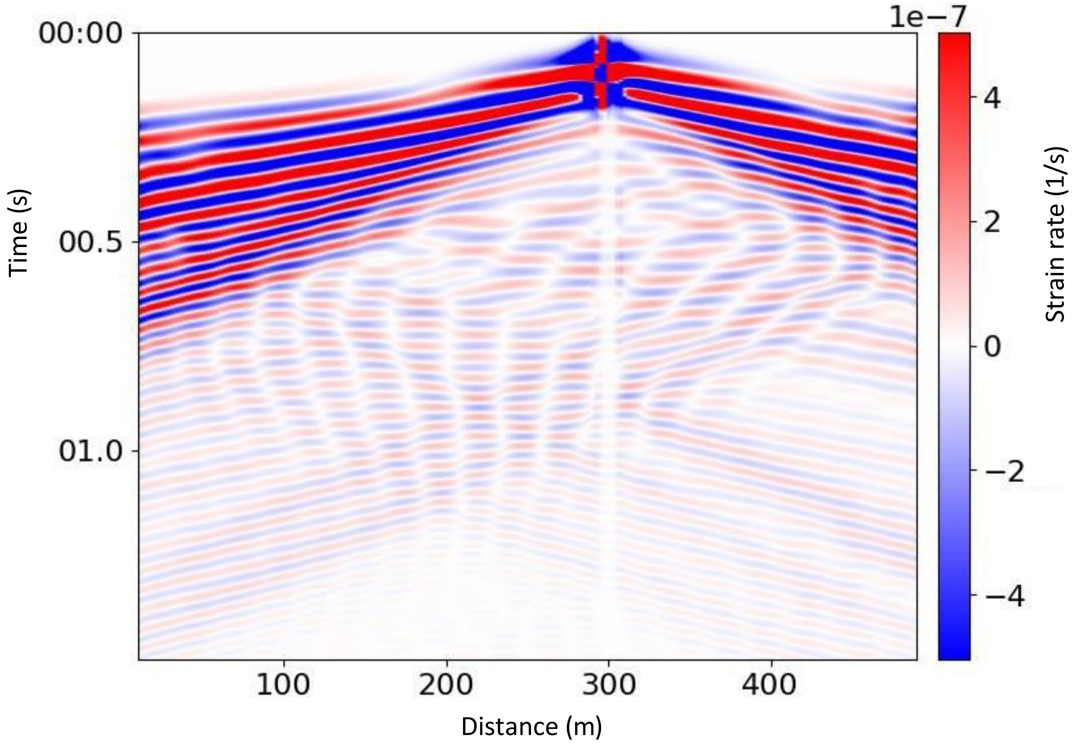


**Figure S6.** Raster plot of the horizontal strain rate response of the array.

Because the explosive source is symmetric, any left–right differences in the recorded strain-rate field arise primarily from geometric asymmetry and lateral velocity contrasts introduced by the ice wedge. The wedge, centered 50 m right of the array mid-point, acts as a localized scatterer and impedance contrast, generating secondary reflected and mode-converted waves. These scattered wavefronts propagate laterally and upward, producing enhanced amplitudes and interference patterns. Consequently, the left sub-array (0-250 m) exhibits slightly delayed but higher-amplitude scattered coda following the main Rayleigh train, while the right array (250-500 m, directly above the wedge) shows more complex near-field interactions and partial shadowing immediately beneath the source. This asymmetric energy distribution emphasizes the strong sensitivity of near-surface wavefields to even modest lateral heterogeneity in permafrost or frozen-soil conditions.

**Text S5.**

**MASW Dispersion Images on Sub-Arrays**

To probe directionality and lateral heterogeneity, we compute frequency-apparent velocity dispersion images separately over two sub-apertures:

- Left sub-array (Figure S7): 0–250 m (operationally 10–250 m due to the applied boundary condition)
- Right sub-array (Figure S8): 250–500 m (operationally 250–490 m due to the applied boundary condition)

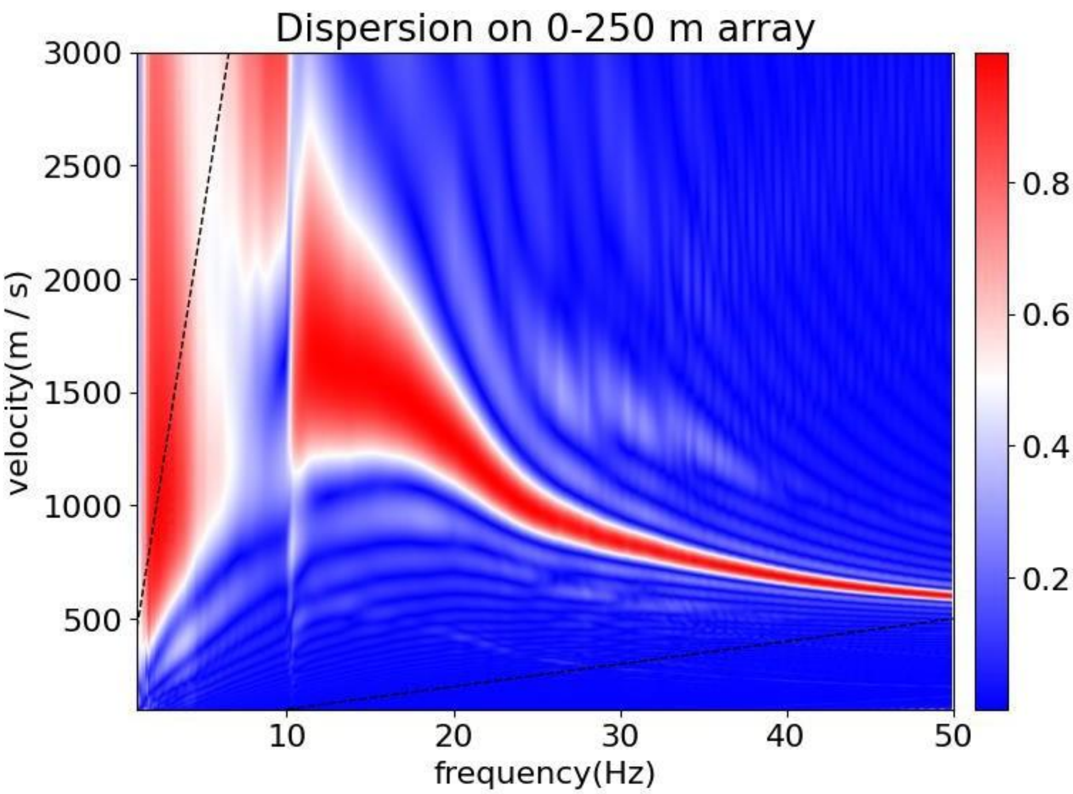


**Figure S7.** Dispersion image of the left sub-array. The dashed lines indicate the minimum and maximum wavelength limits.

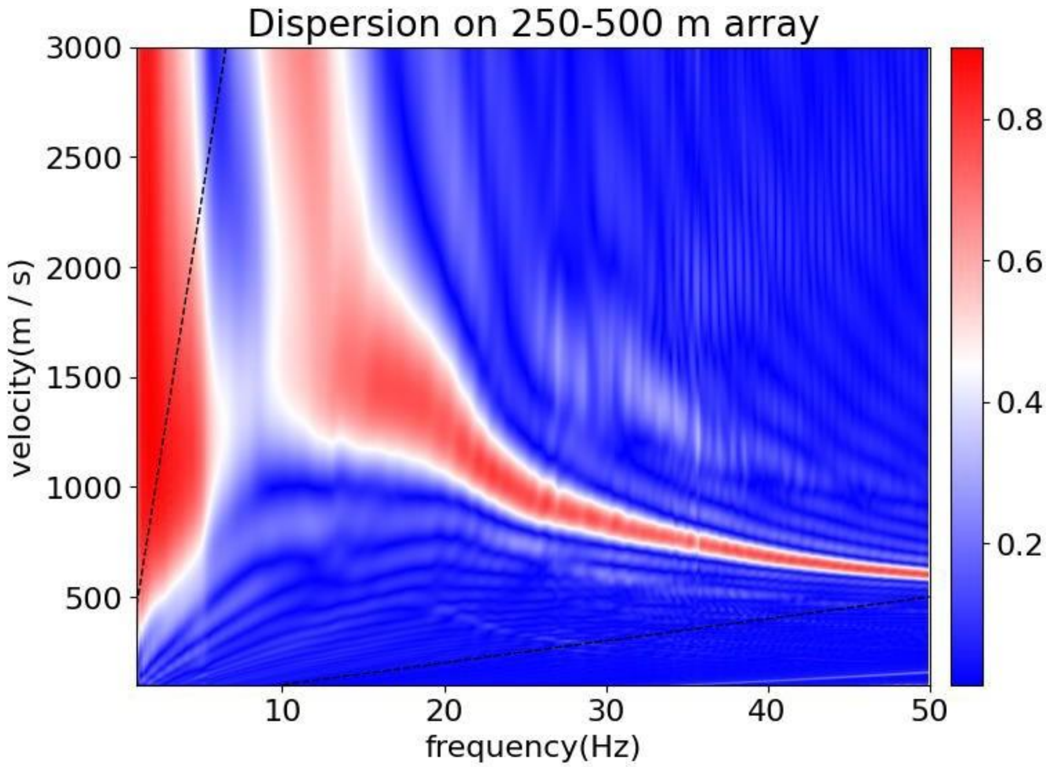


**Figure S8.** Dispersion image of the right sub-array. The dashed lines indicate the minimum and maximum wavelength limits.

Even considering one relatively small ice wedge, both halves show a clear, continuous fundamental Rayleigh mode, but the right sub-array (with ice wedge) exhibits broader energy lobes and slightly higher low-frequency phase velocity. The left sub-array represents a narrower and cleaner dispersion moveout. However, the right sub-array shows enhanced higher-mode energy (10–30 Hz), indicative of local impedance contrast and surface-wave multipathing.

The right sub-array exhibits concentration of the lowest frequencies at slightly higher apparent velocities than the left side, indicating local stiffening of the near-surface materials. The overall bandwidth remains comparable between the two sides, although coherence is marginally reduced on the right. In contrast, the left sub-array shows mild distortion in the lower-frequency range around 10 Hz, likely caused by scattering of long-wavelength energy from the ice wedge as it propagates toward the more distant receivers. These observations demonstrate that lateral heterogeneity can induce measurable left–right asymmetry in dispersion characteristics, expressed through phase-velocity bias, increased modal complexity, and dispersion branch broadening.

Furthermore, to accentuate the scattering effects of the ice wedge, the wedge base was increased to 100 m, and the source was relocated inside the wedge at x=300m and a depth of 5 m. Under these conditions, the resulting dispersion image (Figure S9) exhibits a discontinuous moveout around 25 Hz and a complete loss of coherence above 30 Hz. This disruption of modal continuity reflects the strong scattering and mode conversion induced by the highly heterogeneous velocity field within and beneath the ice wedge. The internal impedance contrasts between frozen and unfrozen zones promote energy partitioning into scattered body waves and guided modes, reducing the coherence of the Rayleigh-wave fundamental branch. Additionally, frequency-dependent attenuation and phase interference from multiply reflected and mode-converted SV and P components further degrade the dispersion energy concentration at higher frequencies. The influence of higher-order Rayleigh modes also becomes more pronounced in this case, consistent with enhanced ellipticity and strong vertical gradients near the ice–soil interface. These results underscore that large-scale frozen inclusions can substantially distort the surface-wave field, producing apparent dispersion discontinuities and frequency-dependent mode scattering that may mimic strong lateral heterogeneity in permafrost terrains.

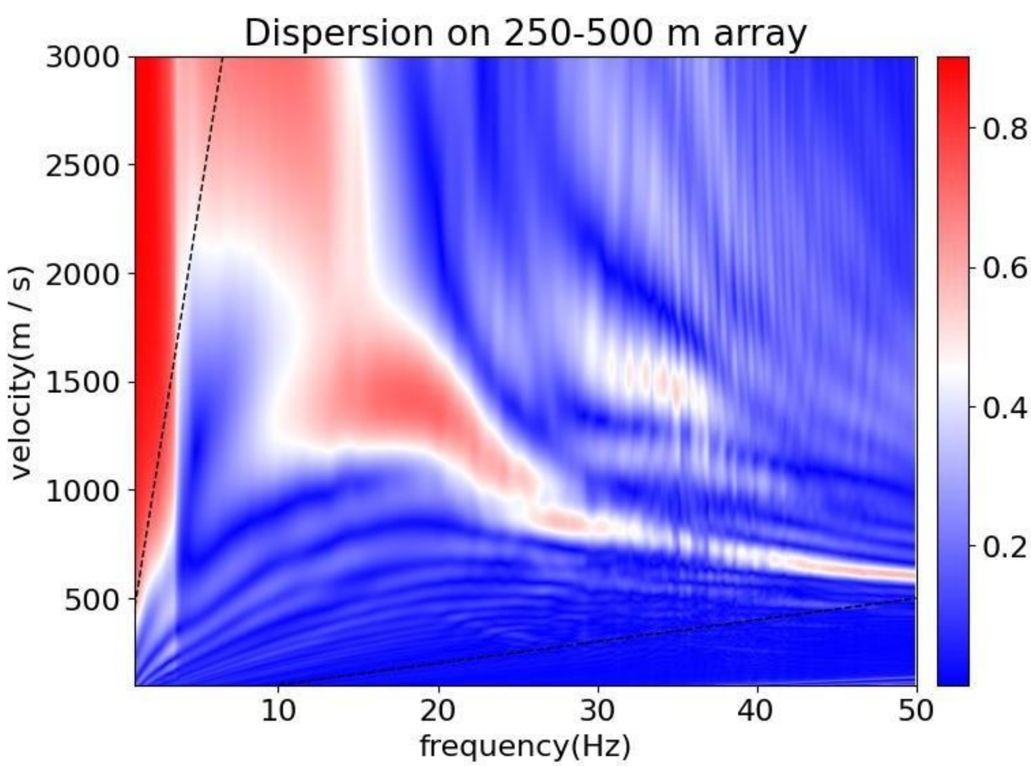


**Figure S9.** The extreme effect of the ice-wedge on the dispersion. The dashed lines indicate the minimum and maximum wavelength limits.